DOI: 10.61782/fa.2025.0493

FORUM ACUSTICUM
EURONOISE 2025

INTRODUCTION OF THE BOOSTLET TRANSFORM FOR ACOUSTIC SIGNAL PROCESSING

Elias Zea[1*]
Marcus Wallenberg Laboratory for Sound and Vibration Research, KTH Royal Institute of Technology, Sweden
zea@kth.se

Marco Laudato[2]
FLOW Centre, KTH Royal Institute of Technology, Sweden
laudato@kth.se

Joakim Andén[3]
Department of Mathematics, KTH Royal Institute of Technology, Sweden
janden@kth.se

ABSTRACT

This paper introduces the boostlet transform to analyze and reconstruct spatiotemporal acoustic fields measured in 2D space-time. The transform builds upon the insight that sparse multi-scale representations learned from natural wavefields perform geometric transformations that preserve the dispersion relation. The boostlet transform decomposes a spatiotemporal wavefield using a collection of wavelet-like functions parametrized by dilations, hyperbolic rotations, and translations in space-time. From a physical viewpoint, boostlets encompass global and localized waveforms with variable band-limited frequency and phase-speed content. We show transform applications of wavefront segmentation and sparse reconstruction of room impulse responses. In particular, we find that boostlet decompositions excel at representing localized wavefront phenomena typical of the early part of such room recordings. At the same time, plane waves perform equally as well as or better than boostlets in the late part.

Keywords: *acoustic signal processing, boostlets, space-time, multi-scale representations, sparse reconstruction.*

1. INTRODUCTION

The accurate analysis and efficient processing of wavefield recordings pose central challenges in acoustic engineering, particularly when dealing with large acoustic spaces. Acoustic field analysis has evolved from early geometrical acoustics models [1–3] to more advanced numerical and data-driven methods. Subsequent studies [4, 5] drew on seismic analogies to refine room-acoustic modeling and extrapolation. At the same time, numerical methods such as finite differences [6], spectral elements [7], and discontinuous Galerkin schemes [8] have become standard tools in acoustics. In recent years, machine learning-based algorithms have allowed the development of new tools for acoustic field analysis. Physics-informed neural networks [9], generative models [10], and neural operators [11] have shown impressive potential thanks to their ability to grasp inherent data structures.

Much less explored is the application of multi-scale directional transformations to acoustic signals in space-time, like the relativistic Poincaré wavelets [12] and the empirical results with shearlets [13] and curvelets [14], which offer optimally sparse representations of the free-space wave propagator [15]. A notable example in this direction is the work by Pinto and Vetterli [16], who introduced directional filter banks to analyze spatiotemporal acoustic fields recorded with 1D microphone arrays. Their approach extends traditional time-frequency analysis by incorporating directionality through spatiotemporal windows, effectively capturing phase-speed content. Nonetheless, directional filter banks cannot account for frequency-dependent behavior emerging from the sources and boundary conditions in the acoustic environment.

A promising approach, as observed empirically in air media [17], is to encode the propagation medium dispersion relation in the definition of the representation system

*Corresponding author: zea@kth.se.

(or *dictionary*) itself. Then, the resulting basis functions become intrinsically aligned with the underlying physics by embedding the dispersion relation in the representation (e.g., through transformations that preserve its geometric definition). Representations of this nature appear to attain *sparser multi-resolution decompositions* and more accurate reconstructions from fewer coefficients [18].

This paper introduces the *boostlet transform* [19] for acoustic signal processing in space-time. The boostlet transform shares mathematical similarities with the Poincaré wavelet transform [12]. The latter performs dilations, hyperbolic rotations, and translations of a mother wavelet-like function; thus, their admissibility condition is the same. However, two distinctions must be made. Firstly, while Poincaré wavelets have been previously applied to relativistic harmonic sources, the focus was not on sparse multi-scale decompositions and efficient reconstruction—the driving purpose of the boostlet transform. Secondly, and as a consequence of the first point, boostlets form a representation system that fulfills Parseval's identity, contrary to Poincaré wavelets, which do not have a scaling function to account for finite dilations and boosts. In previous work [18], we observed that boostlets attain higher accuracy reconstruction from fewer coefficients and superior denoising performance than other multi-scale transforms, such as wavelets and shearlets. The present work studies these properties and the physical consequence of those properties from the perspective of acoustic measurements.

2. BOOSTLET THEORY

The boostlet transform decomposes a wavefield over a dictionary of wavelet-like atoms called *boostlets*. This section defines these functions and the resulting decomposition and reconstruction formulas.

2.1 Boostlets

Boostlets are defined by applying various transformations to a function known as a *mother boostlet*. We denote this function by $\psi(\varsigma)$, where $\varsigma = (x, t)$ is a point in space-time. To obtain a family of boostlet functions from this mother boostlet, we apply a dilation, a hyperbolic rotation (a Lorentz boost), and a translation to obtain

$$\psi_{a,\theta,\tau}(\varsigma) = a^{-1}\psi(M_{a,\theta}^{-1}(\varsigma - \tau)), \tag{1}$$

where

$$M_{a,\theta} = \begin{bmatrix} a\cosh\theta & -a\sinh\theta \\ -a\sinh\theta & a\cosh\theta \end{bmatrix} \tag{2}$$

with a dilation factor $a \in \mathbb{R}_{>0}$, a hyperbolic rotation angle $\theta \in \mathbb{R}$, and a translation vector $\tau \in \mathbb{R}^2$. By varying the parameters a, θ, and τ, we can modify the original waveform $\psi(\varsigma)$ to express different types of waves in space-time.

We can also consider the above transformations in the Fourier domain. Let us define the Fourier transform of a space-time function $f(\varsigma)$ as

$$\widehat{f}(\xi) = \int_{\mathbb{R}^2} f(\varsigma) e^{-2\pi i \xi^{\mathrm{T}} \varsigma} d\varsigma, \tag{3}$$

where $\xi = (k, \omega)$ is a wavenumber–frequency vector. We now divide the wavenumber–frequency plane into three parts: the *near field* where $|\omega| < |k|$, the *far field* where $|k| < |\omega|$, and the *radiation cone* where $|\omega| = |k|$. Acoustically, waveforms in the near field correspond to evanescent waves, while the far field contains propagating waves.

The effect of the dilation, boosting, and translation in the Fourier domain can be described by

$$\widehat{\psi}_{a,\theta,\tau}(\xi) = a e^{-2\pi i \tau^{\mathrm{T}} \xi} \widehat{\psi}(M_{a,\theta}^{\mathrm{T}} \xi). \tag{4}$$

From this relationship, it can be seen that if $\psi(\varsigma)$ is supported in the near-field cone, the same is true for all $\psi_{a,\theta,\tau}(\varsigma)$. As a result, these near-field boostlets can only be used to decompose wavefields that are entirely supported in the near-field cone. We resolve this by defining a far-field version of $\psi(\varsigma)$ as

$$\psi^{\star}(x, t) = \psi(t, x). \tag{5}$$

In other words, we switch the roles of time and space, which moves $\psi(\varsigma)$ from the near to the far field. We can now define the far-field boostlets

$$\psi^{\star}_{a,\theta,\tau}(\varsigma) = a^{-1}\psi^{\star}(M_{a,\theta}^{-1}(\varsigma - \tau)). \tag{6}$$

Together, we will see that these functions form a natural decomposition of wavefields in nondispersive media.

2.2 Building a physical intuition

Boostlets, and similarly Poincaré wavelets, are short, pulse-like waveforms in space-time, parametrized with dilations, corresponding to *spatiotemporal frequency intervals*, and boosts, corresponding to *phase speed intervals*. As illustrated in Fig. 1 below, we can understand the boostlet construction as hyperbolically expanding the Fourier support of a plane wave, which is mapped into a Cartesian grid $(a, \theta) \in \mathbb{R}_{>0} \times \mathbb{R}$ for the far- and near-field cones. Thus, boostlets effectively provide natural,

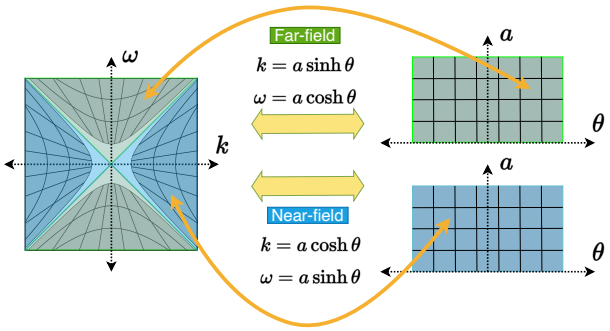

Figure 1: Boostlet partitioning (left) in the Fourier domain and (right) in the dilation-boost domain, (a, θ), via the hyperbolic change of coordinates for the (top-right) far-field cone and (bottom-right) near-field cone.

multi-scale directional decompositions of propagating and evanescent wavefronts in unified space-time. In particular, boostlets localize (extract) wavefronts in space-time when their frequencies and phase speeds match the wavefront location in the (a, θ) domain. This means boostlet decompositions highlight (band-pass filter) wavefronts with certain phase-speed content, accounting for complex, frequency-dependent wave phenomena.

The spatiotemporal frequencies associated with dilations shall not be mistaken for stationary frequencies (i.e., time-harmonic dependence), as this would imply a separate treatment of space-time. On the contrary, these frequencies correspond to hyperbolic frequency bands due to the Lorentz boost parameter $\theta = \operatorname{arctanh}(v_p/c)$, where v_p is the phase speed along the 1D array axis, and c is the sound speed. For $\theta = 0$ in the far-field cone, i.e., $k = 0$, the apex of the hyperbolic frequency band is at $\omega = a$, which corresponds to the frequency of a wavefront propagating with infinite phase speed [20], i.e., normal-incident upon the 1D microphone array. Conversely, for $\theta = 0$ in the near-field cone, i.e., $\omega = 0$, the apex of the hyperbola is at $k = a$, which corresponds to the frequency of an evanescent wavefront propagating with zero phase speed.

2.3 Boostlet decompositions

Together, the near- and far-field boostlets cover the entire wavenumber–frequency plane, $(k, \omega) \in \mathbb{R}^2$, and thus allow us to decompose an arbitrary wavefield without losing information. Concretely, we define the near- and far-field *boostlet coefficients* $Bf(a, \theta, \tau)$ and $B^\star f(a, \theta, \tau)$, respectively, by computing the inner product with the various boostlet functions, yielding

$$Bf(a, \theta, \tau) = \langle f, \psi_{a,\theta,\tau} \rangle \tag{7}$$

and

$$B^\star f(a, \theta, \tau) = \langle f, \psi^\star_{a,\theta,\tau} \rangle, \tag{8}$$

respectively.

The above decomposition presupposes that we decompose the wavefield $f(\varsigma)$ over the boostlets $\psi_{a,\theta,\tau}(\varsigma)$ and $\psi^\star_{a,\theta,\tau}(\varsigma)$ for arbitrarily large dilation factors a. Physically, this means arbitrarily long measurement times. In practice, this is not meaningful as the measurement time is limited (thereby limiting the largest scale A) for a given data type or task. We can therefore restrict a to be in the range $(0, A)$ and capture the remaining part of the wavefield using a *boostlet scaling function* $\phi_A(\varsigma)$ that satisfies

$$|\widehat{\phi}_A(\xi)|^2 = 1 - \int_{(0,\,A)\,\times\,\mathbb{R}} |\widehat{\psi}_{a,\theta,0}(\xi)|^2 + |\widehat{\psi}^\star_{a,\theta,0}(\xi)|^2 \frac{\mathrm{d}a\mathrm{d}\theta}{a}, \tag{9}$$

fulfilling Parseval's relation. We translate $\phi_A(\varsigma)$ to obtain $\phi_{A,\tau}(\varsigma - \tau)$ and the *boostlet scaling coefficients* are then given by

$$Sf(A, \tau) = \langle f, \phi_{A,\tau} \rangle. \tag{10}$$

2.4 Boostlet expansions

It can be shown that we can now recover the original wavefield $f(\varsigma)$ from these coefficients through the formula [18, 19]

$$\begin{aligned} f(\varsigma) = &\int_{\mathbb{R}^2} Sf(A, \tau)\phi_{A,\tau}(\varsigma)\mathrm{d}\tau \\ &+ \int_{(0,\,A)\,\times\,\mathbb{R}\,\times\,\mathbb{R}^2} Bf(a, \theta, \tau)\psi_{a,\theta,\tau}(\varsigma)\frac{\mathrm{d}a\mathrm{d}\theta\mathrm{d}\tau}{a^3} \\ &+ \int_{(0,\,A)\,\times\,\mathbb{R}\,\times\,\mathbb{R}^2} B^\star f(a, \theta, \tau)\psi^\star_{a,\theta,\tau}(\varsigma)\frac{\mathrm{d}a\mathrm{d}\theta\mathrm{d}\tau}{a^3}. \end{aligned} \tag{11}$$

While the above derivations are performed for continuous wavefields and boostlets, we deal with discrete data in practice. Therefore, the integrals are replaced by the appropriate sums, and the values of the parameters a, θ, and τ are sampled on discrete grids. An example of a possible mother boostlet (and the family of boostlet functions it generates) is found in Zea *et al.* [19]. Fig. 2 below shows a boostlet dictionary with $n_a = 2$ discrete scales and $n_\theta = 3$ discrete boosts.

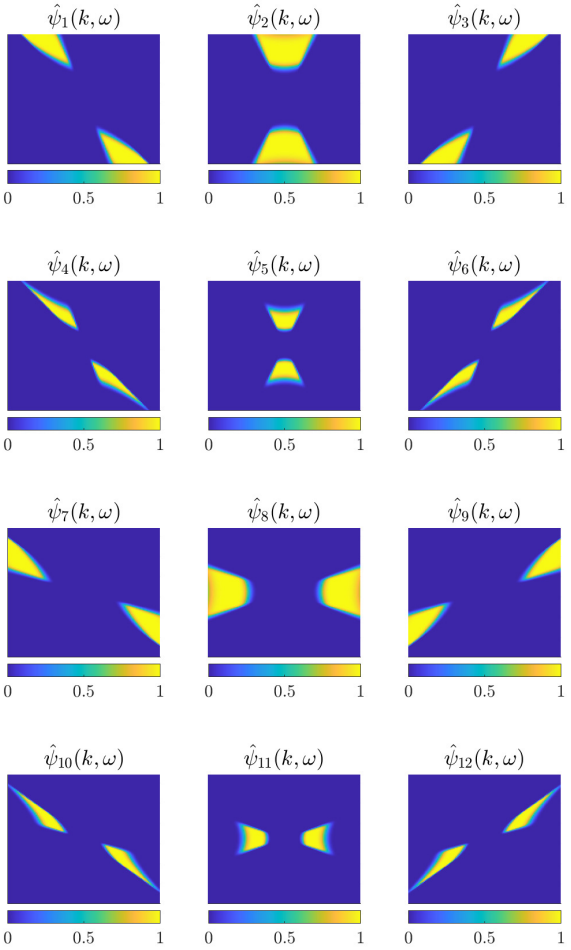

(a) Boostlets in the Fourier domain.

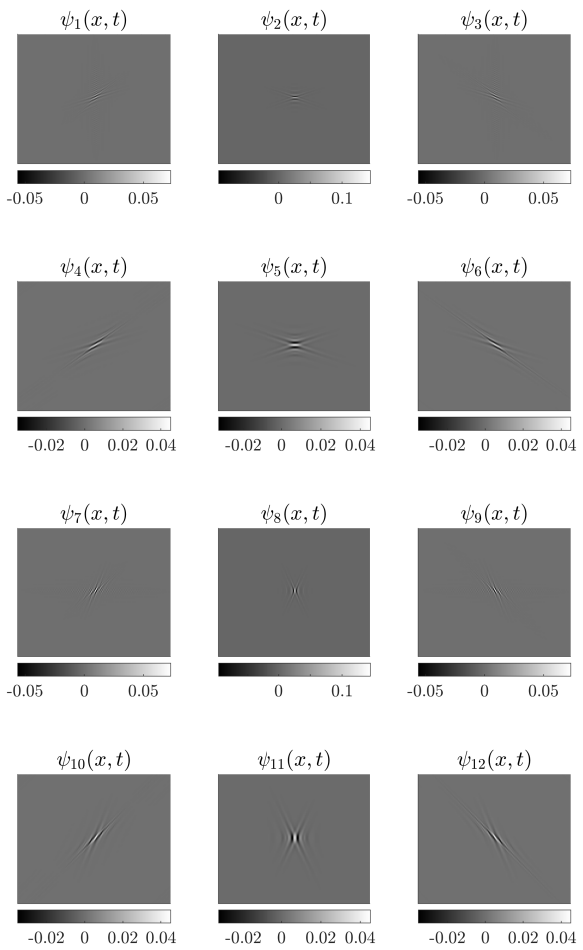

(b) Boostlets in space-time.

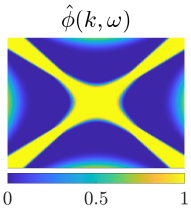

(c) Scaling function in the Fourier domain.

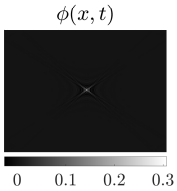

(d) Scaling function in space-time.

Figure 2: A $128 \times 128 \times 13$ boostlet dictionary with $n_a = 2$ discrete scales and $n_\theta = 3$ discrete boosts. The first two rows of (a) and (b) correspond to far-field boostlets, while the last two rows correspond to near-field boostlets. The boostlet scaling function is shown in (c) and (d).

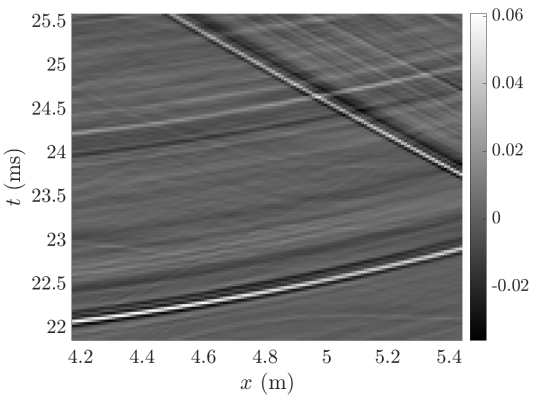

Figure 3: 128 × 128 spatiotemporal room impulse response in the NBI Auditorium A [21].

3. WAVEFIELD ANALYSIS

In this section, we analyze 2D spatiotemporal acoustic fields using discrete boostlets. We use the room impulse response (RIR) dataset measured by Figureoa *et al.* at the Niels Bohr Institute (NBI) in Denmark [21]. The RIRs have been obtained along two lines in the spatial domain, with microphone spacing of $\Delta_x = 1$ cm. The sound source emitted exponential frequency sweeps from 20 Hz to 20 kHz, with a sampling frequency of 48 kHz. The reader is referred to the documentation in [21] for more details on the measurements. To properly sample the dispersion relation of air (i.e., so that the far- and near-field cones fit exactly within the 2D Fourier grid), we pre-process the RIRs by re-sampling them in time to the sampling frequency $f_s = c/\Delta_x \approx 34.3$ kHz.

We consider a 128×128 wavefield in space-time from the NBI RIR dataset. We shall denote such a pressure signal with p. Fig. 3 below depicts the acoustic pressure amplitude in space-time. It can be observed that it consists of a combination of two dominant wavefronts.

When we apply the boostlet dictionary in Fig. 2 to the wavefield in Fig. 3, we obtain the boostlet coefficients shown in Fig. 4 via the inner products $\langle p, \psi_{j,\tau} \rangle, j = 1, i \ldots 12$, and $\langle p, \phi_\tau \rangle$ for translation vectors τ on a 2D grid. It can be seen that the coefficients resulting from the inner products $\langle p, \psi_{2,\tau} \rangle$, $\langle p, \psi_{3,\tau} \rangle$, $\langle p, \psi_{5,\tau} \rangle$, $\langle p, \psi_{6,\tau} \rangle$, and $\langle p, \phi_\tau \rangle$ have much larger real-part amplitudes than those of the remaining inner products. In particular, the inner products with $\psi_{2,\tau}$ and $\psi_{5,\tau}$ appear to localize the first wavefront in Fig. 3. Similarly, the inner products

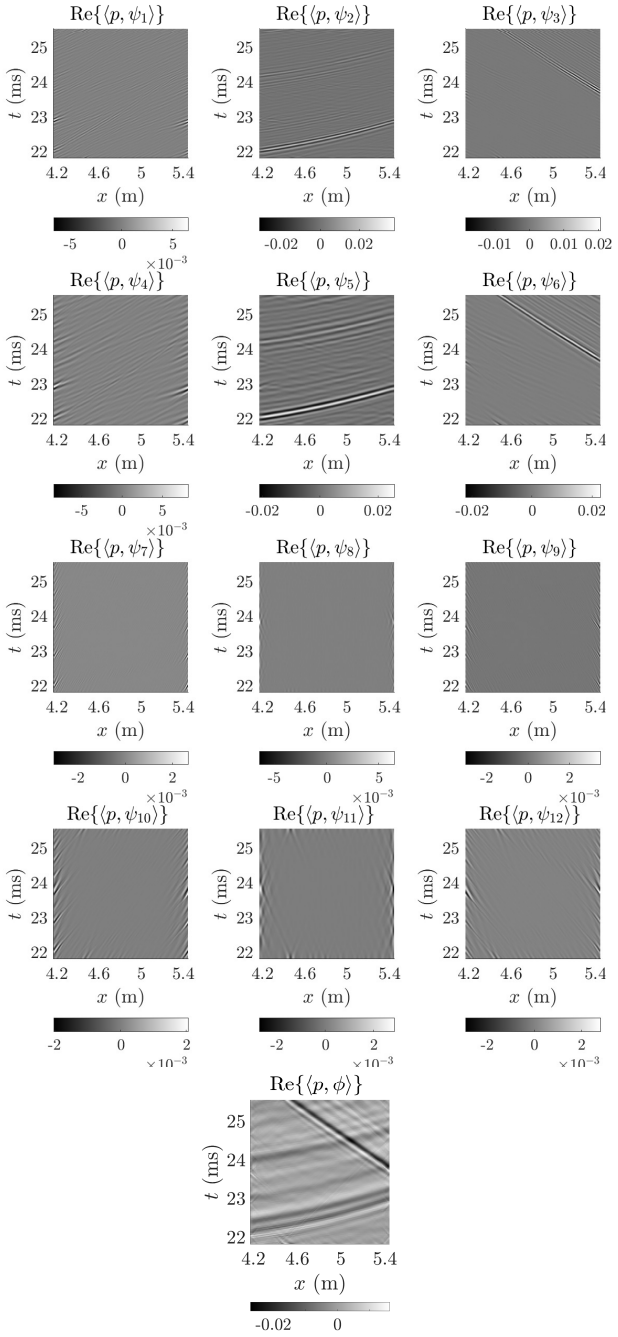

Figure 4: Boostlet decomposition of the acoustic field in Fig. 3 using the dictionary in Fig. 2.

with $\psi_{3,\tau}$ and $\psi_{6,\tau}$ seem to localize the second dominant wavefront from the right-hand side of the x axis. Finally,

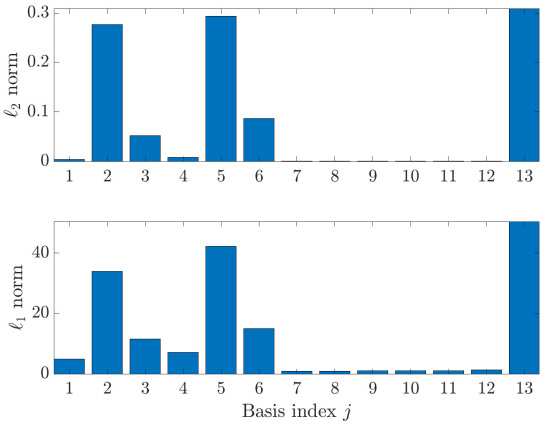

Figure 5: ℓ_2 and ℓ_1 norms of the boostlet coefficients across space-time per index $j = 1, \ldots, 13$, using the boostlet dictionary in Figure 2.

the inner products with ϕ_τ yield a smoothened version of the original wavefield with high-frequency content corresponding to phase speeds near the speed of sound (i.e., oblique incidence over the array). This is understood by looking at the shape of $\hat{\phi}(k, \omega)$ in Fig. 2(c).

At a higher level, we can analyze the ℓ_2 and ℓ_1 norms—$\|\cdot\|_q = [\sum_i |\cdot_i|^q]^{1/q}$ for $q = 1, 2$—of the boostlet coefficients across all space-time translations. Fig. 5 shows these norms, indexed with j representing the jth boostlet function for all translations $\tau \in [0, 1, \ldots, 127]^2$. The index $j = 13$ corresponds to the boostlet scaling function coefficients $\langle p, \phi_\tau \rangle$. Remarkably, the ℓ_2 norms reveal that the energy is concentrated on the inner products with the boostlets $\psi_{2,\tau}$, $\psi_{3,\tau}$, $\psi_{5,\tau}$, and $\psi_{6,\tau}$, and with the scaling function ϕ_τ. Conversely, the remaining coefficients are significantly smaller in ℓ_2 and ℓ_1 norms, particularly the evanescent coefficients associated with $\psi_{7,\tau}, \ldots, \psi_{12,\tau}$. As shown in Fig. 4, these evanescent components are most active at the boundaries of the space-time window, suitable to account for periodicity effects introduced by FFTs.

Implementing segmentation entails synthesizing the acoustic field in space-time from the boostlet coefficients that capture a given wavefront, say, $\psi_{2,\tau}$ and $\psi_{5,\tau}$, to reconstruct the first wavefront in Fig. 3. Then, set all boostlet coefficients with associated indices $j \neq \{2, 5\}$ to zero and perform an inverse boostlet transform. These results highlight the boostlet transform's potential to separate and quantify individual wavefronts from room impulse response recordings.

4. SPARSE WAVEFIELD RECONSTRUCTION

This section shows the result of reconstructing acoustic fields using boostlets. We use plane wave decompositions in space-time as a comparison method via 2D fast Fourier transforms (FFTs). Given the distinct nature of plane wave decompositions and boostlets, we shall not compare their performance solely based on quantitative metrics but also on qualitative reconstruction.

We aim to solve a *basis pursuit denoising* problem of the form [22]:

$$\min_{\alpha} \frac{1}{2}\|p_\delta - \Phi\alpha\|_2^2 + \mu\|\alpha\|_1, \tag{12}$$

where $p_\delta = p + \delta$ is the pressure wavefield with noise δ, here a zero-mean Gaussian-distributed with a given signal-to-noise ratio (SNR), Φ is a synthesis operator (e.g., inverse Fourier/boostlet transform), $\alpha_\bullet$ contains the transform-domain coefficients ($\bullet = \mathrm{pw}$ or bt for plane waves and boostlets, respectively), and $\mu > 0$ is a regularization parameter that balances data fidelity and sparsity.

To solve (12), we employ an iterative soft-thresholding algorithm [23], using FFTs to implement Φ and its adjoint efficiently, and the L-curve [24] to find the optimal μ. This process assumes that the noise variance is known or has been estimated. Finally, we set the maximum thresholding iterations to 200, a log-space of 250 values for $\mu \in [10^{-4}, 5 \cdot 10^{-1}]$, and we assess the reconstruction performance by computing the relative root-mean-squared error $\epsilon_\bullet = \|p - p_\bullet\|_2 / \|p\|_2 \times 100\%$ (again with $\bullet = \mathrm{pw}$ or bt).

Fig. 6 shows the reconstruction of noisy wavefields in the early and late parts of the RIRs using plane waves and boostlets. In the early part shown in Fig. 6(a), plane wave reconstructions contain artifacts at the edges of the space-time window, which arise due to a lack of wavefield periodicity. In contrast, boostlet reconstructions account for non-periodic, localized behavior more effectively and yield a smaller relative reconstruction error. We attribute this extended performance to the evanescent boostlets.

The reconstructions in the late RIR part shown in Fig. 6(b) suggest that the performance is the opposite. We find a natural explanation for this performance in terms of Sommerfeld's radiation boundary condition. A spherical wavefront in an early window of 128×128 space-time samples spreads its energy and becomes locally planar in a later window of the same size. Another per-

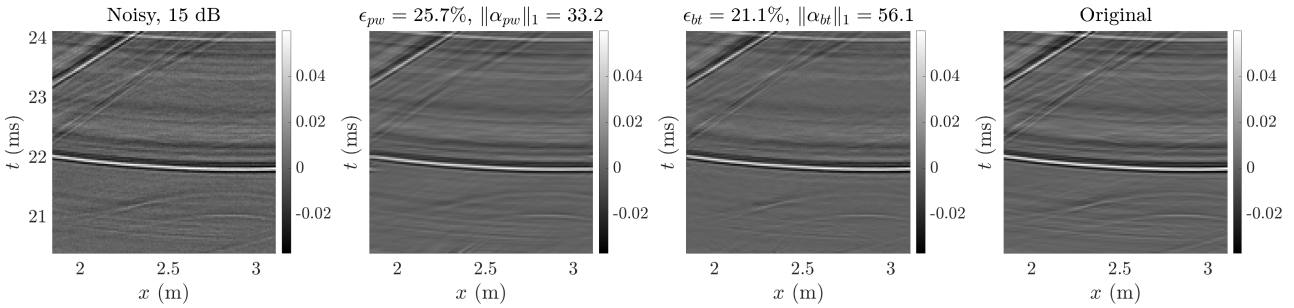

(a) Reconstruction of a space-time wavefield in the early part.

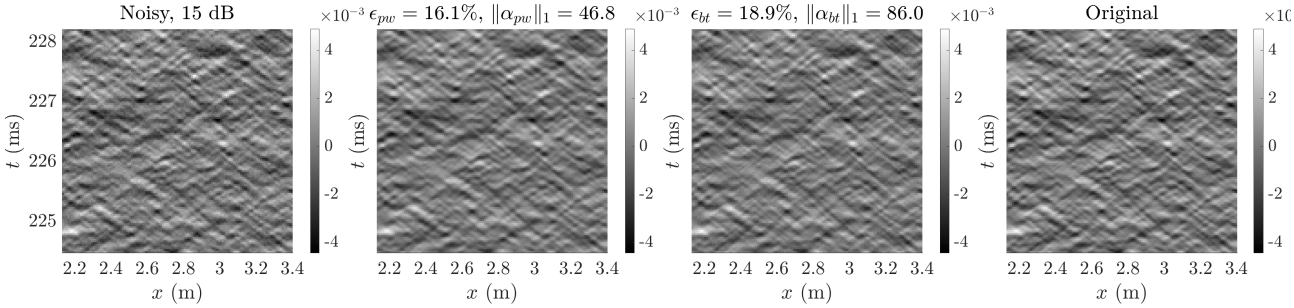

(b) Reconstruction of a space-time wavefield in the late part.

Figure 6: Reconstruction of noisy acoustic wavefields in the (a) early and (b) late part. Left column: Noisy wavefield, SNR $=$ 15 dB. Middle-left column: Reconstructions with plane waves. Middle-right column: Reconstructions with boostlets. Right column: Reference wavefield.

spective is that the early RIR part likely has more spherical/aperiodic wavefronts than the late part, which is more diffuse and carries wavefronts propagating with multiple phase speeds.

5. CONCLUDING REMARKS

The boostlet transform provides a natural, multi-scale directional decomposition of wavefield data in space-time. Boostlet transforms decompose wavefields into a collection of waveforms parametrized with the Poincaré group and dilations. Potential applications of boostlets for multi-scale wavefront segmentation are discussed. Compared to plane waves, the boostlet transform tested in this work excels at sparsely reconstructing wavefield phenomena in the early part of room impulse responses. We find that boostlets effectively capture localized wavefronts due to wave scattering and periodicity effects. Further research entails compressed sensing of acoustic fields and feature-extraction for machine-learning algorithms.

6. ACKNOWLEDGMENTS

E.Z. acknowledges the financial support of the Swedish Research Council, grant agreement No. 2020-04668.

7. REFERENCES

[1] M. R. Schroeder, B. S. Atal, and C. Bird, "Digital computers in room acoustics," in *Proc. 4th ICA, Copenhagen M*, vol. 21, 1962.

[2] A. Krokstad, S. Strøm, and S. Sørsdal, "Calculating the acoustical room response by the use of a ray tracing technique," *J. Sound Vib.*, vol. 8, no. 1, pp. 118–125, 1968.

[3] J. Allen and D. Berkley, "Image method for efficiently simulating small-room acoustics," *J. Acoust. Soc. Am.*, vol. 65, pp. 943–950, 1979.

[4] A. J. Berkhout, D. de Vries, and J. J. Sonke, "Array technology for acoustic wave field analysis in enclo-

sures," *J. Acoust. Soc. Am.*, vol. 102, no. 5, pp. 2757–2770, 1997.

[5] A. J. Berkhout, D. de Vries, J. Baan, and B. W. van den Oetelaar, "A wave field extrapolation approach to acoustical modeling in enclosed spaces," *J. Acoust. Soc. Am.*, vol. 105, no. 3, pp. 1725–1733, 1999.

[6] B. Hamilton and S. Bilbao, "FDTD Methods for 3-D Room Acoustics Simulation With High-Order Accuracy in Space and Time," *IEEE/ACM Trans. Audio Speech Lang. Process.*, vol. 25, no. 11, pp. 2112–2124, 2017.

[7] F. Pind, A. P. Engsig-Karup, C.-H. Jeong, J. S. Hesthaven, M. S. Mejling, and J. Strømann-Andersen, "Time domain room acoustic simulations using the spectral element method," *J. Acoust. Soc. Am.*, vol. 145, pp. 3299–3310, 06 2019.

[8] H. Wang, I. Sihar, R. Pagán Muñoz, and M. Hornikx, "Room acoustics modelling in the time-domain with the nodal discontinuous Galerkin method," *J. Acoust. Soc. Am.*, vol. 145, pp. 2650–2663, 04 2019.

[9] X. Karakonstantis, D. Caviedes-Nozal, A. Richard, and E. Fernandez-Grande, "Room impulse response reconstruction with physics-informed deep learning," *J. Acoust. Soc. Am.*, vol. 155, no. 2, pp. 1048–1059, 2024.

[10] E. Fernandez-Grande, X. Karakonstantis, D. Caviedes-Nozal, and P. Gerstoft, "Generative models for sound field reconstruction," *J. Acoust. Soc. Am.*, vol. 153, pp. 1179–1190, 02 2023.

[11] N. Borrel-Jensen, S. Goswami, A. P. Engsig-Karup, G. E. Karniadakis, and C.-H. Jeong, "Sound propagation in realistic interactive 3D scenes with parameterized sources using deep neural operators," *Proc. Natl. Acad. Sci. U.S.A.*, vol. 121, no. 2, p. e2312159120, 2024.

[12] M. V. Perel, "Integral representation of solutions of the wave equation based on Poincaré wavelets," in *Proc. International Conference Days on Diffraction 2009*, pp. 159–161, 2009.

[13] E. Zea, "Compressed sensing of impulse responses in rooms of unknown properties and contents," *J. Sound Vib.*, vol. 459, p. 114871, 2019.

[14] F. J. Herrmann and G. Hennenfent, "Non-parametric seismic data recovery with curvelet frames," *Geophys. J. Int.*, vol. 173, pp. 233–248, 04 2008.

[15] E. J. Candès and L. Demanet, "The curvelet representation of wave propagators is optimally sparse," *Commun. Pure Appl. Math.*, vol. 58, no. 11, pp. 1472–1528, 2005.

[16] F. Pinto and M. Vetterli, "Space-time-frequency processing of acoustic wave fields: Theory, algorithms, and applications," *IEEE Trans. Signal Process.*, vol. 58, no. 9, pp. 4608–4620, 2010.

[17] E. Zea and M. Laudato, "On the representation of wavefronts localized in space-time and wavenumber-frequency domains," *JASA Express Letters*, vol. 1, no. 5, p. 054801, 2021.

[18] E. Zea, M. Laudato, and J. Andén, "Sparse wavefield reconstruction and denoising with boostlets," in *Proc. International Conference on Sampling Theory & Applications (SampTA)*, 2025.

[19] E. Zea, M. Laudato, and J. Andén, "A continuous boostlet transform for acoustic waves in space-time," *arXiv preprint arXiv:2403.11362*, 2024.

[20] E. G. Williams, *Fourier Acoustics: Sound Radiation and Nearfield Acoustical Holography*. San Diego: Academic Press, 1999.

[21] A. Figueroa-Duran, X. Karakonstantis, S. A. Verburg, and E. Fernandez-Grande, "Room Impulse Response Dataset: Niels Bohr Institute - Auditorium A ," Nov. 2024.

[22] S. S. Chen, D. L. Donoho, and M. A. Saunders, "Atomic decomposition by basis pursuit," *SIAM J. Sci. Comput.*, vol. 20, no. 1, pp. 33–61, 1998.

[23] I. Daubechies, M. Defrise, and C. De Mol, "An iterative thresholding algorithm for linear inverse problems with a sparsity constraint," *Commun. Pure Appl. Math.*, vol. 57, no. 11, pp. 1413–1457, 2004.

[24] P. C. Hansen, *Rank-Deficient and Discrete Ill-Posed Problems: Numerical Aspects of Linear Inversion*, ch. Ch. 7, Parameter-Choice Methods, pp. 175–208. Philadelphia, USA: SIAM, 1 ed., 1998.